Probing excited-state dynamics of transmon ionization

Zihao Wang,[1] Benjamin D'Anjou,[2] Philippe Gigon,[2] Alexandre Blais,[2,3] and Machiel S. Blok[1,*]

[1] *Department of Physics and Astronomy, University of Rochester, Rochester, NY 14627*
[2] *Institut Quantique and Département de Physique, Université de Sherbrooke, Sherbrooke J1K 2R1 QC, Canada*
[3] *CIFAR, Toronto, M5G 1M1 Ontario, Canada*

(Dated: May 2, 2025)

The fidelity and quantum nondemolition character of the dispersive readout in circuit QED are limited by unwanted transitions to highly excited states at specific photon numbers in the readout resonator. This observation can be explained by multiphoton resonances between computational states and highly excited states in strongly driven nonlinear systems, analogous to multiphoton ionization in atoms and molecules. In this work, we utilize the multilevel nature of high-E_J/E_C transmons to probe the excited-state dynamics induced by strong drives during readout. With up to 10 resolvable states, we quantify the critical photon number of ionization, the resulting state after ionization, and the fraction of the population transferred to highly excited states. Moreover, using pulse-shaping to control the photon number in the readout resonator in the high-power regime, we tune the adiabaticity of the transition and verify that transmon ionization is a Landau-Zener-type transition. Our experimental results agree well with the theoretical prediction from a semiclassical driven transmon model and may guide future exploration of strongly driven nonlinear oscillators.

I. INTRODUCTION

The ability to perform fast, high-fidelity, quantum nondemolition (QND) measurements is essential for quantum error correction and, more generally, for any quantum circuit that requires mid-circuit measurement. The standard method to qubit measurement in superconducting circuits is dispersive readout [1, 2]. In this approach, a superconducting qubit, e.g., transmon [3] or fluxonium [4], weakly coupled to a far-detuned resonator, induces a state-dependent frequency shift to the resonator. A qubit measurement is performed by exciting the resonator with a readout tone, such that the field in the resonator entangles with the qubit, resulting in a projection of the qubit state as the field is detected [5]. In principle, this process is QND, and the signal-to-noise ratio within a given time can be improved by increasing the amplitude of the resonator field. Recent experiments have achieved over 99% assignment fidelity on transmons with readout times equal to or less than 100 ns [6–10]. Despite this progress, readout errors continue to be a major bottleneck in achieving fault-tolerant quantum computation [11, 12].

An important limitation to dispersive readout in a transmon is that strong drives can excite the transmon outside its computational two-level subspace [6, 10, 13–17] in a process that has been referred to as measurement-induced state transition (MIST) [14] and transmon ionization [16, 18, 19]. Multiphoton qubit-drive resonances have been identified as a source of these transitions [14], and theoretical frameworks capable of predicting their occurrence have been developed [14, 17, 18, 20–22]. These tools have also been applied to the fluxonium [23–25] and to develop methods for mitigating ionization [26–29]. This phenomenon bears some resemblance to multiphoton ionization in atoms and molecules, where a strong laser or microwave field promotes the electron from a bound state into the continuum [30–35]. In both cases, the system can be driven into a highly excited state with delocalized wavefunctions and energies above the confining potential.

A comprehensive understanding of these multiphoton processes is a key step in developing strategies to avoid unwanted transitions in dispersive readout. While experimental results are consistent with theoretical predictions for the critical photon number of transmon ionization, other features—such as the final state reached and the occurrence of Landau-Zener dynamics—remain unverified. It is challenging to observe these phenomena since the control and measurement of typical transmons are often limited to the 4 lowest states, excluding the highly excited states. In this work, we study these unexplored features of transmon ionization by directly measuring its excited-state dynamics using high-E_J/E_C transmons that enable high-fidelity control and readout of 10 energy eigenstates [36, 37]. In the regime of negative transmon-resonator detuning, we demonstrate that the transmon ionization is indeed a pairwise transition between a qubit state and a highly excited state. We identify which states are populated, the critical photon number at which ionization happens, and the amount of population transfer during ionization. We find that both semiclassical dynamics simulations and Floquet analysis are in excellent agreement with our experimental results, confirming that the semiclassical driven transmon model can successfully capture the main features of ionization dynamics. Finally, using pulse-shaping techniques to control the photon number in the resonator, we tune the system through the multiphoton resonance condition at variable speed and verify that the transmon ionization is

* machielblok@rochester.edu

a Landau-Zener-type transition where more population is ionized during an adiabatic process.

II. IONIZATION OF HIGH-E_J/E_C TRANSMONS

The mechanism of transmon ionization can be understood as a multiphoton resonance in a driven transmon. The drive induces an ac-Stark shift to each transmon eigenstate, resulting in a resonance when the energy difference between two shifted transmon states equals an integer number of the drive photon energy [14, 17, 18, 20–22]. As a result, a driven transmon can transition from its computational subspace to a highly excited state at a specific drive amplitude. In principle, these resonances can occur between many pairs of transmon states and for a variety of transmon parameters. In practice, however, typical transmons that have relatively shallow potential are often excited to a state close to the top of the potential, as shown in Fig. 1(a), and such a highly excited state is harder to address experimentally due to charge noise. Transmon ionization to highly excited states has thus far only been observed indirectly as a leakage out of the qubit subspace. In contrast, the high-E_J/E_C transmons in our experiments have deeper potentials and confine more energy levels; see the right-hand side of Fig. 1(a). As a result, at least 10 transmon eigenstates are insensitive to charge noise and can be controlled and measured [36, 37]. This enables us to directly probe excited-state dynamics of transmon ionization. In the right of Fig. 1(a), we show an example level diagram where the transmon levels are ac-Stark shifted, and n photons in the drive are absorbed to cause transition between $|1\rangle$ and $|7\rangle$, as will be the case in Sec. III.

The dynamics of the transmon-resonator system under an external drive is governed by the Hamiltonian ($\hbar = 1$) [1, 3]

$$\begin{aligned}\hat{H}(t) = 4E_C(\hat{n}_t - n_g)^2 - \sum_{m=1}^{M} E_{Jm}\cos(m\hat{\varphi}_t) \\ + \omega_r \hat{a}^\dagger \hat{a} - ig(\hat{n}_t - n_g)(\hat{a} - \hat{a}^\dagger) \\ - i\varepsilon(t)\cos(\omega_d t)(\hat{a} - \hat{a}^\dagger).\end{aligned} \tag{1}$$

In this expression, E_{Jm}, E_C, $\hat{n}_t$, $\hat{\varphi}_t$ and n_g are respectively the Josephson energies, the charging energy, the charge operator, the phase operator, and the offset charge of the transmon. Moreover, ω_r and $\hat{a}$ are the bare frequency and annihilation operator of the resonator, while $\varepsilon(t)$ and ω_d are the amplitude and frequency of the capacitive drive on the resonator, respectively. The resonator has a linewidth κ. In the dispersive regime, it inherits a transmon-state-dependent frequency shift χ_j as well as Kerr $K_{r,|j\rangle}$ and higher-order nonlinearities for any nonzero coupling strength g [1]. Equation (1) includes higher harmonics of the Josephson potential that provide a more accurate description of the transmon spectrum [36, 38]. Two high-E_J/E_C transmons are used in this work, Q_A with $E_{J1}/E_C = 275$ and Q_B with $E_{J1}/E_C = 235$. For both transmon-resonator pairs, the qubit frequency is lower than the resonator frequency; see Appendix A for the full set of parameters.

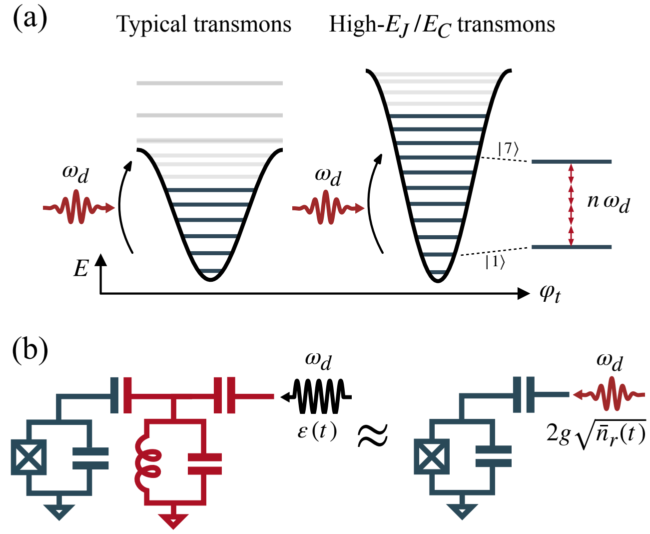

FIG. 1. Transmon ionization concepts. (a) The potentials and eigenstates of transmons. Here, we show examples of two transmons with $\omega_{01}/2\pi = 5\,\text{GHz}$ and $E_J/E_C = 100$ (left) or $E_J/E_C = 270$ (right). The target state of ionization for a typical transmon is often close to (or even above) the top of its potential. High-E_J/E_C transmons have a deeper potential and confine more energy levels, which makes the highly excited states accessible during the transmon ionization. The level diagram depicts a multiphoton resonance. In this example, the energy levels of states $|1\rangle$ and $|7\rangle$ are ac-Stark shifted by the drive to reach the resonance condition $\tilde{\omega}_7 - \tilde{\omega}_1 = n\omega_d$ at a certain drive power, with ω_d the drive frequency and n the number of absorbed photons. Typically, $n > 1$. (b) Circuit diagrams. When the transmon is in one of its eigenstates, a readout pulse with frequency ω_d and amplitude $\varepsilon(t)$ creates a coherent state in the resonator. This coherent state can be effectively modeled as a classical drive applied directly to the transmon, which can induce transitions between transmon states. This driven transmon model is used for the numerical simulations in this work; see Eq. (2).

Because of this choice of qubit-resonator detuning and the weak transmon-resonator coupling strength $g/2\pi \sim 30\,\text{MHz}$, the dispersive shifts are small, and ionization occurs at large photon numbers in these devices [22]. As a result, the dimension of the full transmon-resonator Hilbert space required to model and simulate the experiment is prohibitively large. However, previous works have shown that the coherent state $\alpha(t)$ in the resonator generated by the readout tone approximately results in an effective classical drive acting on the transmon [17, 20, 22, 39]; see Fig. 1(b). In that case, the effective semiclassical Hamiltonian for the transmon is

$$\hat{H}_{\rm sc}(t) = 4E_C(\hat{n}_t - n_g)^2 - \sum_{m=1}^{M} E_{Jm}\cos(m\hat{\varphi}_t) \\ - 2g\sqrt{\bar{n}_r(t)}\sin[\omega_d t - \phi(t)](\hat{n}_t - n_g), \tag{2}$$

where the resonator field is written as $\alpha(t) = \sqrt{\bar{n}_r(t)}e^{i\phi(t)}$ with $\bar{n}_r(t) = |\alpha(t)|^2$ being the average photon number. Transmon ionization occurs at specific values of $\bar{n}_r$, corresponding to a set of critical photon numbers for each transmon eigenstate $|j\rangle$. This model neglects quantum fluctuations in the resonator and, in particular, measurement-induced dephasing. Nevertheless, as discussed below, it captures experimental observations after the results are averaged over gate charge.

III. EXPERIMENTAL IDENTIFICATION OF TRANSMON IONIZATION

We first show the excited-state populations for the ionization of Q_A. The sequence of our experiment is shown in Fig. 2(a). At the beginning of the sequence, the transmon is prepared in one of its eigenstates $|j\rangle$. Then, a 2.2 µs square stimulation pulse is sent to the resonator. The frequency of this pulse is chosen to be on resonance with the dressed resonator frequency $\omega_d = \omega_{r,|j\rangle}$ at zero photon number. The stimulation is followed by a 10 µs ($\sim 6.5/\kappa$) ring-down and then the end-sequence measurement. We calibrate the mean photon number $\bar{n}_r$ from the ac-Stark shift $(\chi_{j+1} - \chi_j)\bar{n}_r$ using a 40 ns spectroscopy pulse on the transmon. By changing the timing of the spectroscopy pulse, the time-dependent $\bar{n}_r(t)$ can be measured; see Fig. 2(b). Because of the relatively small linewidth κ, the resonator does not reach a steady state during the stimulation pulse and requires a long ring-down time. In this experiment, we use this spectroscopy sequence to calibrate the conversion between stimulation amplitude and maximum mean photon number $\bar{n}_{r,\max}$ at low photon number, up to 400 photons, and extrapolate to higher photon numbers accounting for the induced Kerr nonlinearity. Details of the conversion and the effect of nonlinearity are discussed in Appendix B.

In Fig. 2(c), we show the resulting transmon populations at the end of the sequence for different maximum mean photon numbers $\bar{n}_{r,\max}$ when the transmon is initially prepared in $|1\rangle$. We observe a series of distinct drops in the population of $|1\rangle$ at specific photon numbers. First, at $\bar{n}_{r,\max} \sim 170$, qubit Q_A becomes resonant with a neighboring transmon, leading to an exchange of excitations between the two transmons; see Appendix C for more details. More interestingly, a signature of ionization is visible at $\bar{n}_{r,\max} \sim 880$ where a population drop of $|1\rangle$ coincides with increased populations in several highly excited states. We attribute the fact that multiple excited states are populated to energy relaxation that occurs after ionization. We identify the highest resolvable excited state with a nonzero population as the ionized state, in this case, $|7\rangle$. Indeed, we do not observe population in $|8\rangle$ for this experiment. As will be shown below and in Sec. IV, state $|7\rangle$ is resonant with other states below 880 photons, which could make the transferred population further ionize to higher excited states during the ring-down process. These states are collectively classified as $|9_+\rangle$ and cannot be identified in our experiment.

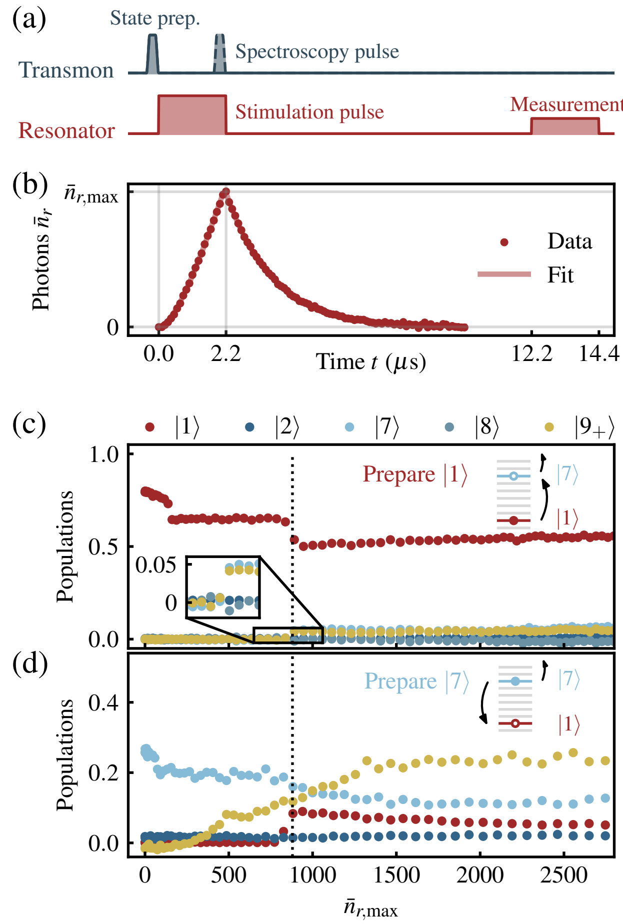

FIG. 2. Transmon ionization experiments. (a) Pulse sequence for the ionization experiments. The transmon is prepared in one of its eigenstates $|j\rangle$ and then evolves under a 2.2 µs stimulation drive on the resonator. After a 10 µs ring-down, a weak multitone readout pulse is applied to measure the transmon populations. At low stimulation power, an optional spectroscopy pulse can be used to probe the mean photon number $\bar{n}_r$. (b) The measured $\bar{n}_r(t)$ for an experiment with $\bar{n}_{r,\max} \sim 150$. (c) Populations of the transmon under different stimulation amplitudes when it is prepared in $|1\rangle$. The vertical dashed line marks the critical photon number at which the $|1\rangle \leftrightarrow |7\rangle$ transition can happen. (d) Populations of the transmon under different stimulation amplitudes when initially prepared in $|7\rangle$. The "deionization" shows the same critical photon number as the upward ionization.

Having experimentally characterized the transmon post-ionization state, we now proceed to further investigate the ionization process. Assuming the $|1\rangle \rightarrow |7\rangle$ transition occurs due to a multiphoton resonant process, the reverse "deionization" process, $|7\rangle \to |1\rangle$, should also be observable at the same resonance condition, i.e., the same critical photon number. Consistent with this expectation, in Fig. 2(d), we prepare the transmon in $|7\rangle$ and indeed observe a population transfer from $|7\rangle$ to $|1\rangle$ at $\bar{n}_{r,\max} \sim 880$. The state $|2\rangle$ is not populated during this process, indicating a direct transition from $|7\rangle$ to $|1\rangle$. We also find a significant population increase in $|9_+\rangle$, which implies strong ionization to higher excited states.

IV. COMPARISONS WITH NUMERICAL SIMULATIONS

We now compare the experimental results to theory. The coupled semiclassical equations for the transmon state $|\psi(t)\rangle$ and the resonator field $\alpha(t)$ in the rotating frame are

$$|\dot{\psi}\rangle = -i\hat{H}_{\mathrm{sc}}(t)\,|\psi\rangle\,, \tag{3}$$

$$\begin{aligned}\dot{\alpha} = &-i(\omega_r - \omega_d)\alpha - \frac{\kappa}{2}\alpha - i\frac{\varepsilon(t)}{2} \\ &+ g(\langle\hat{n}_t\rangle - n_g)e^{i\omega_d t}.\end{aligned} \tag{4}$$

The last term of Eq. (4) describes the backaction of the transmon on the resonator field and captures all transmon-induced resonator nonlinearities within the semiclassical framework. Note that we performed the rotating-wave approximation on the resonator drive $\varepsilon(t)$. Our model does not include transmon relaxation or the weak interaction with the neighboring qubit described above, both of which are observed in the experiment. However, these processes are expected to be most relevant during the slow ring-down, after the multiphoton ionization that is of interest to us has already occurred. Indeed, the relaxation times of the most relevant states are longer or comparable to the duration (12 µs) of the pulse sequence. Moreover, we show in Appendix C that for the high powers at which ionization occurs, population transfer to the neighboring qubit is negligible during the resonator ramp-up.

To highlight the population transfer between the qubit subspace and higher excited states that occurs during the pulse sequence, we report the total population in the qubit subspace $P_{\leq 1}$ and the total population in the leakage subspace $P_{\geq 2}$. We plot these experimentally measured populations as a function of the maximum mean photon number $\bar{n}_{r,\max}$ in Fig. 3 (dots). We investigate two specific multiphoton resonances: the $|0\rangle \leftrightarrow |6\rangle$ resonance in Fig. 3(a, b) and the $|1\rangle \leftrightarrow |7\rangle$ resonance in Fig. 3(d, f).

The theoretical prediction is obtained by numerically solving the coupled semiclassical system in Eqs. (3) and (4). The simulations include the ring-down stage since the residual photons after stimulation can also induce ionization. This is especially true since the resonator field varies more slowly during ring-down, increasing the probability of ionization [18, 22]. The simulation is performed using two distinct models of transmons: the conventional transmon model with a single Josephson harmonic (E_{J1} model) and a model that includes 8 Josephson harmonics (E_{J8} model). The parameters in each model are independently fitted from experimentally measured transmon frequencies [36]. Moreover, because charge sensitive states of the transmon are involved, the

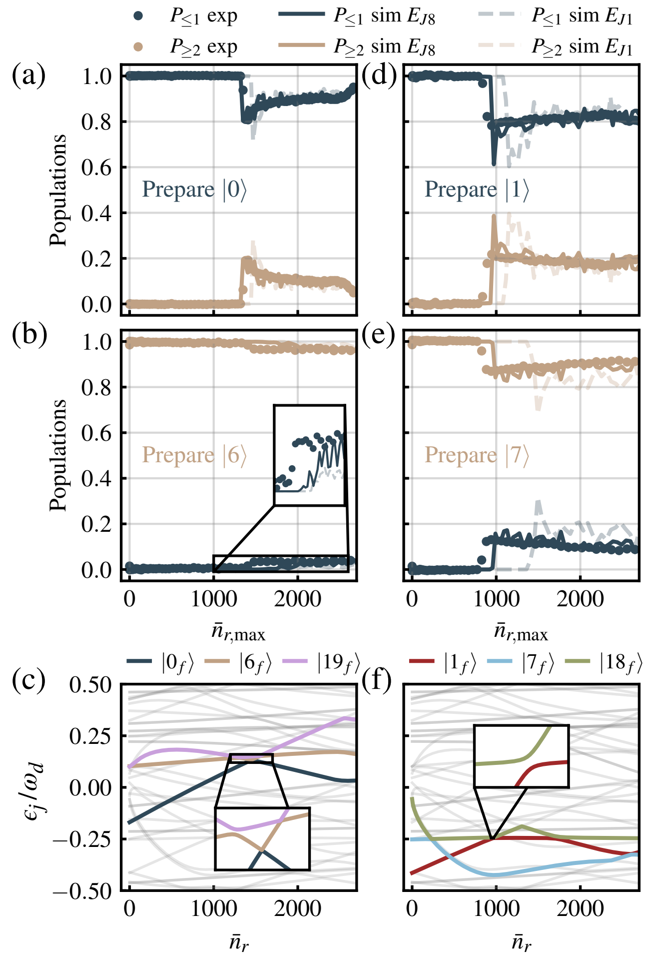

FIG. 3. Comparisons between experiments and numerical simulations. (a-b) Transmon ionization associated with the $|0\rangle \leftrightarrow |6\rangle$ transition. Two different models, the conventional transmon model (E_{J1}, dashed lines) and the Josephson harmonics model (E_{J8}, solid lines), are used in simulations. We show the population of the qubit subspace $P_{\leq 1}$ and the populations of the higher excited states $P_{\geq 2}$. (c) Normalized Floquet quasienergies ϵ_j/ω_d for each transmon branch when $\omega_d = \omega_{r,|0\rangle}$. The $|0_f\rangle$ branch has an avoided crossing with $|6_f\rangle$, which is also coupled to the higher-excited branch $|19_f\rangle$. (d-e) Similar to (a-b) but for the $|1\rangle \leftrightarrow |7\rangle$ transition. (f) Normalized Floquet quasienergies ϵ_j/ω_d for each transmon branch when $\omega_d = \omega_{r,|1\rangle}$. The $|1_f\rangle$ branch has an avoided crossing with the $|18_f\rangle$ branch. The final state found in the dynamical simulations and the experiment is $|7\rangle$ instead of $|18\rangle$. This is due to a weak avoided crossing at lower photon number, at which most of the population in $|18_f\rangle$ is diabatically transferred to $|7_f\rangle$ during ramp-down. We take $n_g = 0$ in (c) and (f).

simulated transition probabilities are averaged over 21 values of n_g in the range $[0, 0.5]$ since we expect our experiments to average over many offset-charge configurations (10^4 repetitions, 20 minutes total run time for each initial state). The simulated transmon populations for the E_{J1} and E_{J8} models are respectively shown as solid and dashed lines in Fig. 3(a,b,d,e).

Both the predicted critical photon number and the amount of population transfer beyond the ionization point are well captured by the simulation using the E_{J8} model, which validates the effectiveness of the aforementioned semiclassical model. We found that for all prepared initial states, the E_{J8} model shows better agreement with experimental data than the E_{J1} model. This is because the resonance conditions for ionization are sensitive to the transmon transition frequencies: Including additional Josephson harmonics in the transmon Hamiltonian plays a key role in accurately predicting the frequency of highly excited states and, thus, the occurrence of transmon ionization.

The ionization process can also be understood via the more intuitive and more computationally efficient Floquet branch analysis [22]. Because the average photon number $\bar{n}_r(t)$ and phase $\phi(t)$ in Eq. (2) vary slowly on the timescale of the drive period $T_d = 2\pi/\omega_d$, the transmon Hamiltonian is approximately periodic on short timescales. As a result, ionization is determined by resonances in the Floquet spectrum associated with the instantaneously periodic Hamiltonian. To obtain this Floquet spectrum, we choose linearly spaced effective transmon drive amplitudes $2g\sqrt{\bar{n}_r}$ in steps of $2\pi\times 100\,\mathrm{kHz}$. For each constant drive amplitude, we calculate the Floquet modes and quasienergies by solving the eigenvalue problem of the propagator $U(T_d, 0)$ for Eq. (2). At $\bar{n}_r = 0$, the result coincides with the bare transmon eigenstates and eigenenergies, from where we sort other Floquet modes and quasienergies at higher amplitudes into a "Floquet branch" for each bare transmon state [22].

We show the normalized quasienergies ϵ_j/ω_d of the Floquet branches for $\omega_d = \omega_{r,|0\rangle}$ in Fig. 3(c) and $\omega_d = \omega_{r,|1\rangle}$ in Fig. 3(f), respectively, highlighting in color the most relevant Floquet branches for the $|0\rangle \leftrightarrow |6\rangle$ and $|1\rangle \leftrightarrow |7\rangle$ resonances. The Floquet branch for a given initial state shows avoided crossings with other branches as $\bar{n}_r$ increases. These avoided crossings indicate the multiphoton transitions responsible for ionization (the quasienergies are defined only modulo ω_d). In general, there are multiple avoided crossings associated with various pairs of Floquet branches. However, we find that the positions of the largest avoided crossings, as well as the branches they involve, are consistent with those observed in the experiments and the dynamical simulations. Once ionization has occurred at these dominant avoided crossings, any number of other avoided crossings involving any of the populated branches can become relevant. This can occur during both the ramp-up and the ring-down phases of the readout pulse sequence.

V. LANDAU-ZENER TRANSITIONS

The avoided crossings in the Floquet quasienergies suggest that transmon ionization is a Landau-Zener-type transition [18, 22]. A Landau-Zener process describes the dynamics of a two-level system evolving under a time-dependent Hamiltonian, where an external control field sweeps the system through an avoided crossing in its spectrum [40, 41]. For transmon ionization, the photon number $\bar{n}_r$ plays the role of this control field, and the adiabaticity of the transition is determined by the speed at which $\bar{n}_r$ crosses the critical photon number [18, 22]. If the transmon is prepared in an eigenstate and traverses an avoided crossing diabatically, ionization does not occur. Conversely, an adiabatic passage results in ionization.

In the experiments shown in Fig. 2, the resonator never reached a steady state, and the adiabaticity was not carefully controlled by the square stimulation pulse. To remedy this, we investigate the Landau-Zener physics of transmon ionization using pulse-shaping techniques applied to transmon Q_B, which has 9 resolvable states. We control the dynamics of the photon number using two different sequences, which we refer to as the steady-state sequence and the Landau-Zener sequence. The measured photon numbers (dots) and the numerical predictions (line) for the two sequences are shown in Fig. 4(a), where all parameters used in the numerical simulations are extracted from independent measurements. Details of the pulse calibration can be found in Appendix D.

In the steady-state sequence, the transmon is initially prepared in $|0\rangle$, followed by a stimulation pulse with three segments; see the top panel of Fig. 4(a). The first segment is a 40 ns ramp-up to rapidly bring the resonator from the vacuum state to the desired photon number $\bar{n}_{r,s}$. The second segment holds the resonator in its steady state with variable duration t_s. The third segment is a 40 ns ramp-down to actively empty the resonator. The frequency of the stimulation pulse is detuned from $\omega_{r,|0\rangle}$ by the expected Kerr shift $\bar{n}_{r,s}K_{r,|0\rangle}$ to compensate for the Kerr effect in the steady state. The short ramping time ensures strong diabaticity during ramping, making the transmon ionization most likely to happen during the steady-state segment. We end the sequence with a 6 µs free ring-down time to fully empty the resonator, followed by a measurement.

The results of the steady-state experiment for different durations t_s and photon numbers $\bar{n}_{r,s}$ are shown in Fig. 4(b). At low photon numbers, the system remains below the critical photon number, and the transmon stays in its initial state $|0\rangle$. At $\bar{n}_{r,s} \approx 1500$, however, the transmon ionizes, with a longer t_s resulting in a lower ground-state population. Following the same method as in Sec. III, we identify the state $|6\rangle$ as one of the post-ionization states, and the transmon is further ionized to higher excited states; see Appendix E. Above the critical photon number, there exists a range of photon numbers where the transition is suppressed again. This is

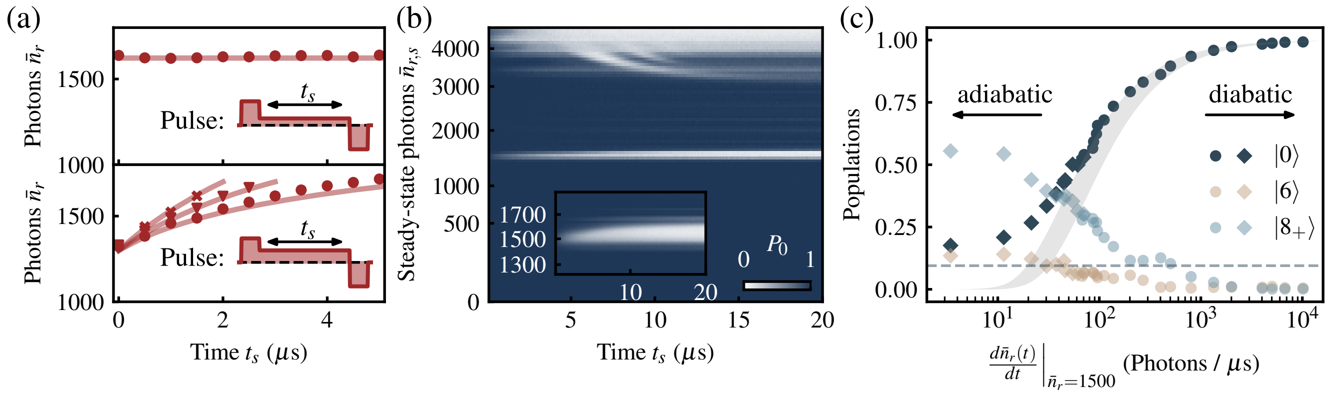

FIG. 4. Landau-Zener transitions. (a) The measured photon numbers (red dots) of the steady-state sequence (top) and Landau-Zener sequence (bottom) for different steady-state times t_s. The data agree well with the numerical prediction (red lines), which uses parameters extracted from independent measurements. The transmon is prepared in $|0\rangle$ at the beginning of the sequence. The insets show the envelopes of the shaped stimulation pulses, each of which includes three segments: ramp-up, steady state, and ramp-down. In the Landau-Zener sequence, the amplitude during t_s is intentionally increased above the amplitude used for the steady-state sequence to drive the resonator from $\bar{n}_{r,i}$ to $\bar{n}_{r,f}$. The pulse is followed by a 6 µs ring-down and an end-sequence measurement. We show three sequences with different Landau-Zener speeds identified by different symbols in the bottom panel. (b) The measured population of $|0\rangle$ from the end-sequence measurement for different steady-state durations t_s and photon numbers $\bar{n}_{r,s}$. We observe a critical photon number for transmon ionization at around 1500 photons (see inset). Above 3000 photons, more resonances appear, while our pulse-shaping method fails to stabilize the photon number due to the higher-order nonlinearities of the resonator. (c) The measured populations of Landau-Zener experiments with different Landau-Zener speeds. The slope $d\bar{n}_r(t)/dt$ is controlled by changing the duration t_s with fixed $\bar{n}_{r,i} = 1300$, $\bar{n}_{r,f} = 1700$ (circles), or by changing the difference $\bar{n}_{r,f} - \bar{n}_{r,i}$ with fixed $t_s = 10$ µs. The horizontal gray dashed line shows the remaining ground-state population P_0 measured in the steady-state experiment, which has $\bar{n}_{r,f} - \bar{n}_{r,i} = 0$. The gray shaded area shows the range of theoretical predictions for 51 evenly spaced values of offset charge n_g. An adiabatic process results in more ionized population.

because the system diabatically crosses the resonance at $\bar{n}_{r,s} \approx 1500$ during the ramping segments while remaining far from other avoided crossings responsible for ionization during the steady-state segment. A similar phenomenon was observed in Ref. [14]. At $\bar{n}_{r,s} > 3000$, there is again a reduction in the ground-state population. This occurs because the higher-order nonlinearities of the resonator become too strong for our pulse to stabilize the photon number for a long time while more avoided crossings appear. As a result, the resonator photon number sweeps through strong resonances, and most of the population eventually transfers from $|0\rangle$ to higher excited states.

Having identified the critical photon number for ionization, we next perform Landau-Zener experiments. The Landau-Zener sequence differs from the steady-state sequence in two ways; see the bottom panel of Fig. 4(a). First, after rapidly filling $\bar{n}_{r,i}$ photons into the resonator, the pulse amplitude of the steady-state segment is adjusted so that the photon number $\bar{n}_r(t)$ increases from $\bar{n}_{r,i}$ to $\bar{n}_{r,f}$ during the time t_s. As a result, the slope $d\bar{n}_r(t)/dt$ near the avoided crossing can be controlled by changing either t_s or $\bar{n}_{r,f} - \bar{n}_{r,i}$. Second, for each slope, the pulse frequency is numerically optimized to compensate for the average Kerr effect during all segments; see Appendix D 4. The Landau-Zener speed near the avoided crossing is thus determined by the slope $d\bar{n}_r(t)/dt$ close to the critical photon number $\bar{n}_r \approx 1500$, with a flat (steep) slope corresponding to an adiabatic (diabatic) process. To reach a wide range of Landau-Zener speeds, we use two different parameterizations of the slope. In the diabatic region, we fix $\bar{n}_{r,i} = 1300$ and $\bar{n}_{r,f} = 1700$, while sweeping the duration t_s from 40 ns to 13 µs. In the adiabatic regime, we fix $t_s = 10$ µs and sweep the difference $\bar{n}_{r,f} - \bar{n}_{r,i}$ while keeping the mean photon number constant, $(\bar{n}_{r,f} + \bar{n}_{r,i})/2 = 1500$. The measured final populations of state $|0\rangle$, state $|6\rangle$, and the combined populations of states $|8\rangle$ or higher are shown in Fig. 4(c) for both the diabatic region (circles) and the adiabatic region (diamonds). More details about the Landau-Zener sequence and its parameterizations can be found in Appendix D 4.

The general trend of our experimental results matches the expectation of Landau-Zener physics, where a more adiabatic transition causes more population to be ionized. The remaining population P_0 in the adiabatic region approaches the result measured in the steady-state experiment, shown as the gray dashed line in Fig. 4(c). To obtain a quantitative comparison between the experiment and the theory, we use Floquet branch analysis. Similar to the method used in Sec. IV, we first calculate the Floquet spectrum at different photon numbers and sort them into Floquet branches. The related avoided crossings are identified by diabatically following the ground-state Floquet branch up to $\bar{n}_r = 2100$. We then select the avoided crossing with the largest gap Δ_{ac} and compute the Landau-Zener diabatic transition probability $P_{\mathrm{LZ}} = \exp(-\pi\Delta_{\mathrm{ac}}^2/2v)$. Here, the speed v describes the rate of change of the gap near the avoided crossing and can be obtained from the Floquet branches and the experimentally measured $d\bar{n}_r(t)/dt$ [22]. This transition probability corresponds to the ground-state population P_0 after the sequence. Because the Floquet spectrum depends on the offset charge n_g, the gray shaded area in Fig. 4(c) shows a range of probabilities calculated by choosing 51 different values of n_g. We find that the theoretical prediction reproduces the experimental trend very well, especially in the diabatic region. In the adiabatic region, the theoretical prediction increasingly deviates from the observed values as the Landau-Zener speed is lowered, because the time spent near the avoided crossing becomes increasingly comparable to the relaxation time of the excited states involved in ionization. The fully coherent Landau-Zener formula is thus not expected to accurately describe the transferred population.

VI. DISCUSSION AND OUTLOOK

The transmon ionization is a key bottleneck for achieving fast, high-fidelity, high-QNDness measurement, which is necessary for many tasks in quantum information processing. In this work, we studied the excited-state dynamics of ionization in high-E_J/E_C transmons. The deep potentials of such transmons enable control and readout of a large number of excited states, which allows us to observe the rich dynamics of ionization. As an example, for our parameters, we identify $|7\rangle$ as one of the target states when the transmon is prepared in $|1\rangle$. This identification is further verified by investigating the reverse "deionization" process from $|7\rangle$ to $|1\rangle$. The photon numbers at which the transitions happen are consistent with each other, indicating the resonant nature of such processes.

Our work further validates the effectiveness of the driven transmon model and Floquet analysis. The comparison between the experimental results and the dynamical simulations shows excellent agreement for both the critical photon numbers and the ionized population. The Schrödinger equation simulation captures the majority of the experimental features. Additional effects, such as measurement-induced decay and dephasing, require additional consideration, which we leave for future work. Our results also highlight the importance of Josephson harmonics for an accurate prediction of the transmon spectrum. Combined with computationally efficient Floquet analysis, ionization could be mitigated by optimizing the transmon and resonator parameters, such as the transition frequencies and the coupling strength, so that the threshold of ionization is increased. This threshold informs the maximum allowable photon number during readout, as shown in Ref. [26], which helps avoid unwanted transitions.

The Landau-Zener physics is another strong evidence of the two-level resonance. Using a pulse-shaping method, we demonstrate precise control of the photon number in the resonator, which allows us to pass through an avoided crossing over a wide range of adiabaticity. Our experimental results agree with the theoretical prediction that a more adiabatic process yields more population transfer. An intriguing question to answer in the future is whether a high-power QND readout is achievable by crossing the resonance diabatically. Moreover, the reported population in Fig. 4(c) corresponds to the transition probability for a single passage through the avoided crossing, and it could be possible to observe Landau-Zener-Stückelberg interference upon a double passage in future work.

Although ionization is often discussed in the context of qubit readout, related challenges can become more significant when using a transmon as a high-dimensional qudit [36, 37], since higher excited states introduce additional resonance conditions in the spectrum. An example is shown in Fig. 2(d), where population transfer between $|7\rangle$ and $|9_+\rangle$ occurs earlier than between $|7\rangle$ and $|1\rangle$. In addition, multitone readout—typically required for qudits [36, 42]—leads to more complex ionization dynamics that cannot be captured by modeling the transmon as being driven by a single periodic tone. These observations highlight the need for careful consideration of readout pulse parameters in qudit applications.

The ability to control higher-energy levels of the transmon may also help in the investigation of ionization in alternative readout approaches, such as longitudinal readout [29, 43] and balanced cross-Kerr readout [28]. Moreover, although this work focuses on measurement-induced effects, similar effects are expected to arise in other contexts where the essential ingredients for ionization are present—namely, strong drives and nonlinearity— such as parametric gates, qubit reset, and quantum state stabilization. Since these scenarios often involve transmon-like circuits, we expect that our work will provide new insights into the effect of strong drives on superconducting quantum circuits beyond readout.

ACKNOWLEDGMENT

We thank Alexander McDonald, Cristóbal Lledó, and Marie Frédérique Dumas for fruitful discussions. We thank Rayleigh William Parker for assistance in designing the sample.

This work is supported by a collaboration between the US DOE and other Agencies. This material is based upon work supported by the U.S. Department of Energy, Office of Science, National Quantum Information Science Research Centers, Quantum Systems Accelerator. Additional support is acknowledged from Air Force Office of Scientific Research Grant No. FA9550-23-1-0121, NSERC, the Ministère de l'Économie et de l'Innovation du Québec, and the Canada First Research Excellence Fund. Devices used in this work were fabricated and provided by the Superconducting Qubits at Lincoln Laboratory (SQUILL) Foundry at MIT Lincoln Laboratory, with funding from the Laboratory for Physical Sciences (LPS) Qubit Collaboratory. The traveling-wave parametric amplifier (TWPA) used in this experiment was provided by IARPA and Lincoln Labs.

Appendix A: Device parameters

The device parameters used in this work are shown in Table I. The two transmons used here are relabeled from the Q_5 and Q_4 in Ref. [36]. The control and stimulation pulses are generated using 16-bit DACs in the Qblox QCM-RF module, and the readout signals are generated and detected using the Qblox QRM-RF module.

Appendix B: Calibration of $\bar{n}_{r,\max}$ for the square stimulation pulse

In Sec. III of the main text, we show the transmon populations as a function of the maximum photon number reached during the sequence. In practice, the experiments were performed by sweeping the instrument amplitude. For a small range of values, this amplitude is typically proportional to the drive amplitude ε on the resonator. For a classical linear resonator initialized in the vacuum state and evolving under a resonant drive, the mean intra-resonator photon number $\bar{n}_r(t)$ at a given time t is

$$\bar{n}_r(t) = \left(\frac{\varepsilon}{\kappa}\right)^2 (1 - e^{-\kappa t/2})^2, \tag{B1}$$

where κ is the decay rate of the resonator. Equation (B1) suggests the quadratic relationship $\bar{n}_r \propto \varepsilon^2$ for a fix time t. However, the actual photon number may deviate from this quadratic behavior due to the Kerr effect.

To find the accurate maximum mean photon number $\bar{n}_{r,\max}$, we first fit the conversion between the instrument amplitude and the measured $\bar{n}_{r,\max}$ at low power. We then extrapolate the photon numbers at higher power based on the driven Kerr resonator model explained in Appendix D. The fitting and extrapolations are repeated for different initial states $|j\rangle$ because the effective κ weakly depends on the state of the transmon [1]. The extrapolation results are shown in Fig. 5(a), where the Kerr coefficient $K_{r,|j\rangle}$ is calculated from numerical diagonalization of the Hamiltonian.

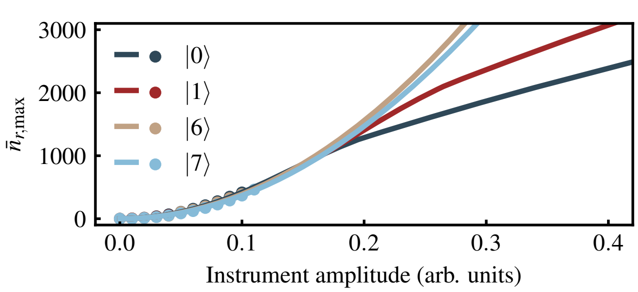

FIG. 5. Measured $\bar{n}_{r,\max}$ and the extrapolation results for initially prepared states $|0\rangle$, $|1\rangle$, $|6\rangle$, and $|7\rangle$.

Appendix C: Interaction with neighbor transmon

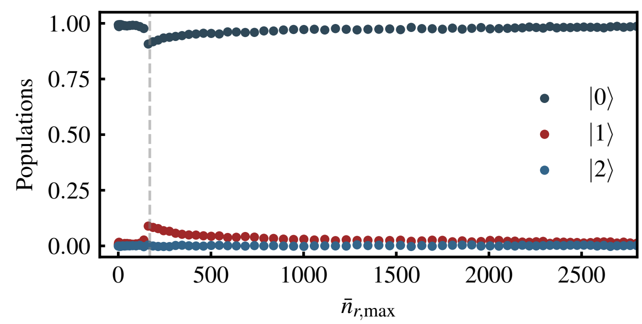

FIG. 6. Eigenstate populations of Q_B for the experimental pulse sequence used in Fig. 2(c) of the main text and in Fig. 5(b).

In Fig. 2 of the main text and in Fig. 5(b), we see a drop in the population of state $|1\rangle$ at $\bar{n}_{r,\max} \sim 170$. We find that it is due to a resonant population swap between Q_A and Q_B, with Q_B remaining idle during this experiment. The two transmons are fabricated on the same chip and designed to have negligible coupling with each other. However, when Q_A is prepared in $|1\rangle$ and ac-Stark-shifted by $-43\,\mathrm{MHz}$, it becomes resonant with the neighbor transmon Q_B, which has the frequency $\omega_{01} = 2\pi \times 4.8380\,\mathrm{GHz}$ at that thermal cycle. This resonance induces a $|10\rangle \leftrightarrow |01\rangle$ swap that causes a population drop in Q_A. In Fig. 6, we show the measured populations of Q_B under different stimulation powers on Q_A using the same experimental sequence as in Fig. 2. The readout pulse on Q_B is added immediately after the stimulation on Q_A to probe transitions that occur during the ramp-up. This also has the benefit of reducing the effect of decay. We find a population peak at around 170 photons, which confirms the occurrence of the resonant swap. This mechanism is further confirmed by the absence of population transfer when preparing the ground state, in which case the swap between the qubits is not energetically possible. Finally, Fig. 6 also shows that the probability of a swap during stimulation becomes small at large photon numbers. This is because the associated resonance is crossed much more rapidly, reducing the probability of a Landau-Zener transition. Thus, at large drive powers, any significant population transfer to Q4 must occur during the ring-down.

TABLE I. Device parameters.

Device Usage	Q_A Sects. III and IV	Q_B Sec. V
First anharmonicity $\alpha_1/2\pi = f_{12} - f_{01}$ (MHz)	-104	-104
0-1 transition frequency $\omega_{01}/2\pi$ (GHz)	4.8817	4.8334
1-2 transition frequency $\omega_{12}/2\pi$ (GHz)	4.7778	4.7198
2-3 transition frequency $\omega_{23}/2\pi$ (GHz)	4.6694	4.6007
3-4 transition frequency $\omega_{34}/2\pi$ (GHz)	4.5557	4.4754
4-5 transition frequency $\omega_{45}/2\pi$ (GHz)	4.4361	4.3428
5-6 transition frequency $\omega_{56}/2\pi$ (GHz)	4.3098	4.2015
6-7 transition frequency $\omega_{67}/2\pi$ (GHz)	4.1753	4.0497
7-8 transition frequency $\omega_{78}/2\pi$ (GHz)	4.0310	3.8848
8-9 transition frequency $\omega_{89}/2\pi$ (GHz)	3.8746	-
Resonator frequency when transmon is at $\|0\rangle$ $\omega_{r,\|0\rangle}/2\pi$ (GHz)	6.470366	6.415708
Dispersive shift $(\omega_{r,\|1\rangle} - \omega_{r,\|0\rangle})/2\pi$ (kHz)	-249	-205
Resonator linewidth $\kappa/2\pi$ (kHz)	105	127
Josephson energy E_{J1}/h (GHz) [a]	29.7	26.8
Charging energy E_C/h (GHz) [a]	0.108	0.116
E_{J1}/E_C [a]	275	235
Transmon-resonator coupling strength $g/2\pi$ (MHz) [a]	31.0	26.5

[a] Parameters here is estimated by E_{J8} model.

Appendix D: Pulse-shaping and calibration for the steady-state and Landau-Zener experiments

The steady-state experiment and the Landau-Zener experiment discussed in Sec. V require precise control over the state of the resonator. In this section, we explain our pulse-shaping method and give examples of numerical simulations and experimental calibration results.

1. Classical resonator model

Consider a classical driven and damped Kerr resonator in a frame rotating at the drive frequency ω_d. The equation of motion of its field $\alpha(t)$ is

$$\begin{aligned}\dot{\alpha}(t) = i\Delta\alpha(t) - iK_r|\alpha(t)|^2\alpha(t) - \frac{\kappa}{2}\alpha(t)\\ - i\frac{\varepsilon(t)}{2}e^{-i\phi_d},\end{aligned} \tag{D1}$$

where $\Delta \equiv \omega_d - \omega_r$ is the drive-resonator detuning, K_r is the Kerr coefficient of the resonator, and $\varepsilon(t)$ and ϕ_d are the amplitude and phase of the drive, respectively. When dispersively coupled to a transmon, the Kerr value is negative due to the negative anharmonicity of the transmon.

2. Linear resonator and three-segment pulse

For a linear resonator ($K_r = 0$) under a constant resonant drive [$\varepsilon(t) = \varepsilon$, $\Delta = 0$], the solution of Eq. (D1) is

$$\alpha(t) = Ce^{-\kappa t/2} - ie^{-i\phi_d}\frac{\varepsilon}{\kappa}, \tag{D2}$$

where C is an integral constant depending on the initial condition. If the resonator starts in the vacuum state, $\alpha(0) = 0$, then

$$\alpha(t) = -ie^{-i\phi_d}\frac{\varepsilon}{\kappa}(1 - e^{-\kappa t/2}), \tag{D3}$$

and the mean photon number reduces to Eq. (B1) with steady-state value $\bar{n}_r = |\alpha(t)|^2 = \varepsilon^2/\kappa^2$. Because it will be useful below, we note that Eq. (D3) is expressed as a real function of time multiplied by a time-independent global phase.

Our goal is to construct a shaped pulse to drive the resonator such that: (a) the resonator is ramped up to its steady state as fast as possible, (b) the steady state is then stabilized for a long time, and (c) the resonator is rapidly ramped down to the vacuum state at the end. We denote the ramp-up, steady state, and ramp-down times as $t_\uparrow$, t_s, and $t_\downarrow$, during which the drive amplitudes $\varepsilon_\uparrow$, ε_s, and $\varepsilon_\downarrow$ are applied, respectively. The drive amplitudes remain constant inside each segment and thus form a step-wise pulse as shown in the inset of Fig. 4(a) in the main text. We emphasize that the sequence is followed by an additional free ring-down with time t_{rd}, which is different from the active ramp-down segment above. This ring-down is added to further ensure the resonator is empty before the final measurement.

To reach the steady state photon number ε_s^2/κ^2 in a given time $t_\uparrow$, the following equality must be satisfied

$$\bar{n}_r(t_\uparrow) = \left(\frac{\varepsilon_\uparrow}{\kappa}\right)^2 (1 - e^{-\kappa t_\uparrow/2})^2 = \frac{\varepsilon_s^2}{\kappa^2}. \tag{D4}$$

If the phase of the pulse is the same for all segments, then Eq. (D4) gives the relation

$$\frac{\varepsilon_\uparrow}{\varepsilon_s} = \frac{1}{1 - e^{-\kappa t_\uparrow/2}} > 1. \tag{D5}$$

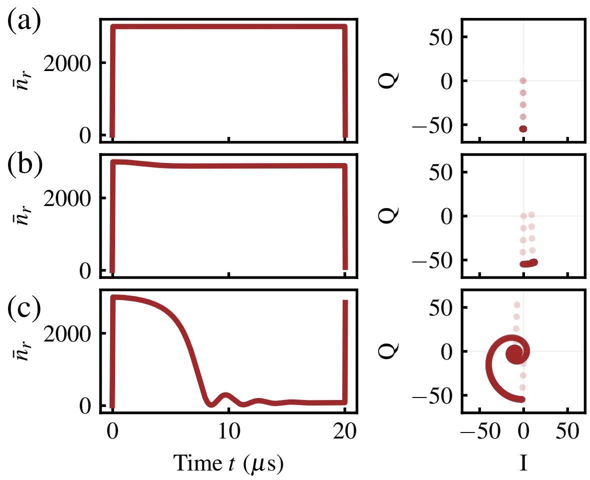

FIG. 7. Numerical simulation of the detuned three-segment pulses. (a) $\Delta = K_r \bar{n}_{r,s}$. (b) $\Delta = 0.93 \times K_r \bar{n}_{r,s}$. (c) $\Delta = 1.07 \times K_r \bar{n}_{r,s}$.

As an example, the resonator R_4 used in this work has $\kappa = 2\pi \times 127\,\mathrm{kHz}$, which requires an amplitude ratio $\varepsilon_\uparrow/\varepsilon_s \approx 63.3$ for a ramp-up time $t_\uparrow = 40\,\mathrm{ns}$.

Similarly, the ramp-down amplitude $\varepsilon_\downarrow$ should satisfy

$$\begin{aligned}\frac{\varepsilon_\downarrow}{\varepsilon_s} &= \frac{e^{-\kappa t_\downarrow/2}}{e^{-\kappa t_\downarrow/2} - 1} \\ &= 1 - \frac{\varepsilon_\uparrow}{\varepsilon_s} < 0, \quad \text{if } t_\uparrow = t_\downarrow.\end{aligned} \tag{D6}$$

3. Kerr resonator and detuning

The pulse introduced in Appendix D 2 can stabilize linear resonators because the drive term in Eq. (D1) balances the damping term. However, the Kerr effect induces field-dependent rotations in the phase plane, such that an initially resonant pulse becomes off-resonant as the field builds up. To balance this effect, we detune the pulse by $\Delta = K_r \bar{n}_{r,s}$ such that it is resonant for the desired steady-state photon number $\bar{n}_{r,s}$. With this choice, the first two terms on the right of Eq. (D1) cancel each other, approximating a linear resonator in the steady state.

As a result of the Kerr effect, the resonant frequency $\omega_r(n_r(t))$ changes during the ramp-up and ramp-down segments, which makes the phase and amplitude of the field deviate from those expected in the linear case. In principle, such deviations can be removed through chirped pulses where the detuning Δ is updated during the ramping, or through calibrating the phase and amplitude of the resulting state after ramping and adjusting the drive accordingly. For simplicity, we keep the same detuning and phase throughout all segments and mitigate the aforementioned problem by reducing the ramping times $t_\uparrow$ and $t_\downarrow$. From Eq. (D5), a shorter ramping time requires a stronger amplitude, and the resulting pulse will have a broader spectrum, which makes it possible for the pulse to remain near-resonant despite the Kerr effect. We choose a 40 ns ramping time, which gives $1/t_\uparrow = 25\,\mathrm{MHz}$. This is much larger than the frequency shift $|\omega_r(n_r = 3000) - \omega_r(n_r = 0)|/2\pi \approx 357\,\mathrm{kHz}$. Here, we take the same time length for ramp-up and ramp-down, $t_\uparrow = t_\downarrow$. We note there are also drawbacks of large amplitude ratio $\varepsilon_\uparrow/\varepsilon_s$, which may cause relatively stronger pulse distortion and also have higher requirements for the resolution of the microwave instrument, such as DACs.

We show numerical simulations of the steady-state pulses in Fig. 7 using experimental parameters. In addition to the case where $\Delta = K\bar{n}_{r,s}$, we also show the results for an under-detuned pulse and an over-detuned pulse, which would be the case for possible miscalibration of the Kerr coefficient or the photon numbers. We find that the under-detuned pulse has better tolerance to such miscalibration, whereas the over-detuned pulse could easily fail to stabilize the photon numbers.

4. Pulse in Landau-Zener sequence

In previous sections, we explained the method to construct the pulse in our steady-state experiments. In our Landau-Zener experiments, we want to control the resonator such that the average photon number changes from $\bar{n}_{r,i}$ to $\bar{n}_{r,f}$ in a given time t_s. Here, we choose the ramping amplitudes such that they correspond to the ramp-up amplitude $\varepsilon_\uparrow$ in a steady-state sequence with $\bar{n}_{r,s} = \bar{n}_{r,i}$ and the ramp-down amplitude $\varepsilon_\downarrow$ in a steady-state sequence with $\bar{n}_{r,s} = \bar{n}_{r,f}$. We leave the amplitude of the quasi-steady-state segment ε_s and the detuning Δ as two free parameters in a numerical optimization for the target pulses. The cost function is designed to minimize the difference between numerical results and the desired average photon numbers, which are $\bar{n}_{r,i}$, $\bar{n}_{r,f}$, and 0 at times $t = t_\uparrow$, $t = t_\uparrow + t_s$, and $t = t_\uparrow + t_s + t_\downarrow$. For relatively short t_s, this method results in monotonically increasing photon number during the quasi-steady-state segment, the derivative of which can be easily extracted.

In the main text, we mention that the Landau-Zener speed is controlled by the slope of the photon number $d\bar{n}_r(t)/dt$. Two different parameterizations are used to adjust the slope, as each of them can only reach a limited range of Landau-Zener speeds. The time-varying parameterization, where we fix $\bar{n}_{r,i} = 1300$ and $\bar{n}_{r,i} = 1700$ and then change the time t_s, fails when t_s becomes comparable to the relaxation time. As a result, the adiabatic region cannot be reached. On the other hand, the number-varying parameterization, where we fix the time $t_s = 10\,\mathrm{\mu s}$, the sum $\bar{n}_{r,i} + \bar{n}_{r,f} = 3000$, and then change the difference $\bar{n}_{r,f} - \bar{n}_{r,i}$, has a maximum allowable difference $|\bar{n}_{r,f} - \bar{n}_{r,i}| < 3000$ and thus a limited diabaticity. It is the combination of the two parameterizations that enables us to explore a wide range of Landau-Zener speeds.

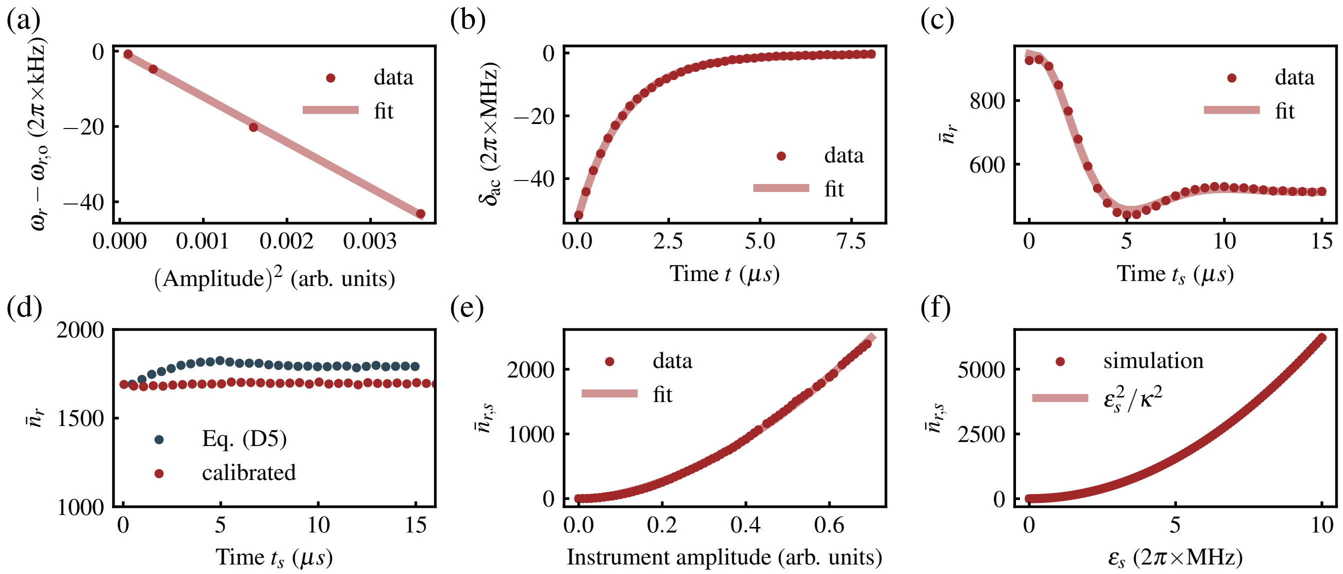

FIG. 8. Calibration results of R_4, which is the resonator used in Fig. 4. (a) Measured resonator frequency and extrapolation at different amplitudes. (b) Free decay measurement to extract the linewidth κ of the resonator. (c) Steady-state experiment with $\Delta = 0$ to extract the Kerr K_r of the resonator. (d) Steady-state experiment with theoretical (blue dots) and calibrated (red dots) ramping amplitude ratio for compensating possible miscalibration and power compression of the experimental apparatus. (e) The measured and fitted relation between the instrument amplitude and the steady-state photon number $\bar{n}_{r,s}$. (f) The analytically calculated and numerically simulated relation between the drive amplitude ε_s and the steady-state photon number $\bar{n}_{r,s}$.

5. Calibration procedures

In this section, we describe the calibration procedures for the steady-state sequence and the Landau-Zener sequence. We show the results for R_4, the readout resonator coupled to Q_B, and we focus on the case where Q_B is prepared in $|0\rangle$ at the beginning of the sequence.

The first step to calibrate the shaped pulse is to measure the resonator frequency at the single-photon level. We perform resonator spectroscopy for various drive amplitudes and fit each spectroscopy result to a Lorentzian function to extract a frequency [36]. The single-photon frequency is then extracted by fitting these frequencies to a quadratic function of the amplitude and then extrapolating to zero amplitude, as shown in Fig. 8(a). The resonator spectroscopy is also used to extract the dispersive shift $\chi_{01} \equiv \omega_{r,|1\rangle} - \omega_{r,|0\rangle} = 2\pi \times -205\,\text{kHz}$.

Due to the finite duration of the spectroscopy pulse, the fitted quality factor may have systematic errors. In such cases, a free decay experiment is preferable to extract the linewidth κ of the resonator. At any time t, we use transmon spectroscopy to measure the ac-Stark shift $\delta_{\text{ac}}(t)$ of the $|0\rangle \leftrightarrow |1\rangle$ transition frequency of the coupled transmon. These ac-Stark shifts are then fitted to an exponential function, as shown in Fig. 8(b), which gives $\kappa_{|0\rangle} = 2\pi \times 127\,\text{kHz}$.

Using the fitted linewidth, we can calculate the ramping amplitude ratio in Eq. (D5). The Kerr coefficient is then measured by applying the three-segment pulse. Here, we set $\Delta = 0$ without any prior knowledge of the value of the Kerr coefficient, and the photon number $\bar{n}_r$ is not stabilized. In that case, the Kerr effect manifests through the time-dependence of $\bar{n}_r(t)$. We calculate the measured photon number using

$$\bar{n}_r(t) = \delta_{\text{ac}}(t)/\chi_{01}, \tag{D7}$$

The results are fitted to the numerical simulation of the three-segment pulse, where the Kerr value K_r, the effective drive amplitude ε_s, and the detuning Δ are treated as fitting parameters, as shown in Fig. 8(c). We leave the detuning Δ as a free parameter to further correct the single-photon frequency extrapolated from Fig. 8(a). As a result, we find $K_{r,|0\rangle} = 2\pi \times -119\,\text{Hz}$.

After calibrating ω_r, κ, K_r, and ε_s, we have the minimal parameters to run the steady-state experiment: we can set $\Delta = K_r(\varepsilon_s/\kappa)^2$ and choose the ramping amplitude ratio based on Eq. (D5). The result is shown as blue dots in Fig. 8(d). Although the photon number is stable for a long time, it does not reach its steady state immediately after the ramp-up segment because the actual amplitude ratio required to be applied on the device may deviate from the theoretical value $\varepsilon_\uparrow/\varepsilon_s \approx 63.3$ that we set to the instrument. Such deviation may come from miscalibration of the linewidth κ or the power compression of the instrument. We correct it by empirically adjusting the amplitude ratio to $\varepsilon_\uparrow/\varepsilon_s = 68.5$, and the result is shown as red dots in Fig. 8(d).

Another consequence of power compression is that the effective drive amplitude ε_s is not proportional to the instrument amplitude. We perform the steady-state experiment at different instrument amplitudes and extract the corresponding steady-state photon numbers $\bar{n}_{r,s}$. The results are fitted to a phenomenological model $y(x) = Ax^m$, and we get $m \approx 1.776 \neq 2$, as shown in Fig. 8(e). This relation gives us the conversion between the instrument amplitude and the $\bar{n}_{r,s}$ reported in Fig. 4(b). We also calculate a similar conversion between the steady-state photon number $\bar{n}_{r,s}$ and the drive amplitude ε_s on the resonator using numerical simulation, as shown in Fig. 8(f). The results agree well with analytical prediction $\bar{n}_{r,s} = \varepsilon_s^2/\kappa^2$.

6. Errors in calibration of photon numbers

In the calibration procedures discussed in Appendix D 5, the photon numbers are extracted using Eq. (D7). This relation is based on the dispersive Hamiltonian. For a multilevel system coupled to a single-mode harmonic oscillator, the dispersive Hamiltonian up to sixth order in perturbation is ($\hbar = 1$)

$$\begin{aligned}\hat{H}_{\mathrm{disp}} &= \sum_j \omega_j \left|j\right\rangle\left\langle j\right| + \omega_r \hat{a}^\dagger \hat{a} \\ &+ \sum_j \chi_j \hat{a}^\dagger \hat{a} \left|j\right\rangle\left\langle j\right| + \sum_j \frac{\eta_j}{2} \hat{a}^\dagger \hat{a}^\dagger \hat{a}\hat{a} \left|j\right\rangle\left\langle j\right| \\ &+ \sum_j \frac{\mu_j}{6} \hat{a}^\dagger \hat{a}^\dagger \hat{a}^\dagger \hat{a}\hat{a}\hat{a} \left|j\right\rangle\left\langle j\right| .\end{aligned} \tag{D8}$$

Below, we discuss possible errors when using this equation.

a. *Kerr effect*

The dispersive Hamiltonian in Eq. (D8) is often truncated to the second order, with the dispersive shift defined as $\chi_{01} = \chi_1 - \chi_0$. However, at large photon numbers, the state-dependent four-wave mixing Kerr η_j and six-wave mixing Kerr μ_j also have non-negligible contributions to the dispersive shift. In other words, the denominator of Eq. (D7) depends on photon number, and the relation between photon number and ac-Stark shift is therefore not linear at large photon numbers.

To estimate the possible errors from these higher-order effects, we calculate the ac-Stark shift δ_{ac} using η_j and μ_j extracted from numerical diagonalization with the parameters shown in Table I. The results are shown in Fig. 9. We find that at 1500 photons, the critical photon number in Fig. 4 of the main text, there could be an underestimation of the photon number of about 100 to 200 photons for a given δ_{ac}.

Because of the existence of μ_j and other higher-order Kerr effects, our choice of detuning for the steady-state experiments, $\Delta = K_r \bar{n}_{r,s}$ as explained in Appendix D 3, fails to stabilize the resonator state at higher photon numbers. An ideal choice of detuning should take into account the nonlinear relation between the dispersive shift and the photon number.

b. *Averaged photon numbers*

Suppose we truncate Eq. (D8) to second order and treat the transmon as a two-level system. In the rotating frame, the Hamiltonian of the system under the spectroscopy pulse can then be simplified to

$$\hat{H}_{\mathrm{spec}}(t) = \frac{1}{2}\left[\Delta - \chi_{01} n_r(t)\right]\sigma_z + \frac{1}{2}\Omega(t)\sigma_x. \tag{D9}$$

Here, $\Delta \equiv \omega_d - \omega_{01}$ is the detuning of the spectroscopy pulse to the qubit frequency, and $\Omega(t)$ is the pulse envelope. In the above expression, we have performed the rotating-wave approximation (RWA). The ac-Stark shift $\delta_{\mathrm{ac}}(t)$ is measured from the excited population $P_{|1\rangle}$ after a spectroscopy pulse of duration T. As a result, the measured $\delta_{\mathrm{ac}}(t)$ reflects the averaged photon number over the time window of the spectroscopy pulse. To see this, we perturbatively calculate the dynamics of the system under Eq. (D9) using average Hamiltonian theory [44]. In this framework, the propagator U is given by

$$\begin{aligned}U(T,0) &= e^{-i\bar{H}_{\mathrm{spec}}T}, \\ \bar{H}_{\mathrm{spec}} &= \bar{H}^{(1)}_{\mathrm{spec}} + \bar{H}^{(2)}_{\mathrm{spec}} + ...,\end{aligned} \tag{D10}$$

where the time-averaged Hamiltonian $\bar{H}_{\mathrm{spec}}$ is expanded at each order in the drive amplitude $\Omega(t)$. Suppose the system is prepared in the ground state $|0\rangle$ before the spectroscopy. The excitation probability to lowest-order in $\Omega(t)$ is

$$\begin{aligned}P_{|1\rangle} &= \left|\left\langle 1\right| e^{-i\bar{H}^{(1)}_{\mathrm{spec}}T}\left|0\right\rangle\right|^2 \\ &= 4\theta^2 \mathrm{sinc}^2\left(\frac{1}{2}\sqrt{\theta^2 + T^2(\Delta - \chi_{01}\bar{n}_r)^2}\right).\end{aligned} \tag{D11}$$

Here, we introduced the rotation angle $\theta \equiv \int_0^T \Omega(t)dt$ and the time-averaged photon number $\bar{n}_r \equiv 1/T \int_0^T n(t)dt$.

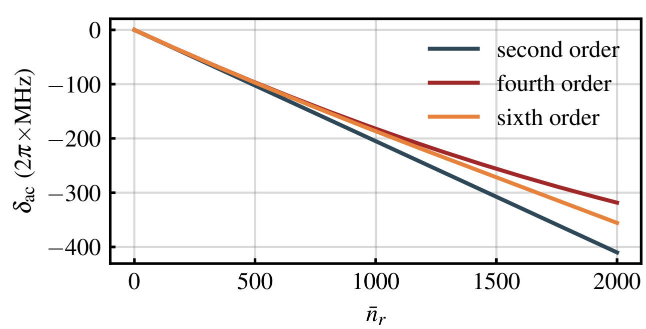

FIG. 9. Estimated ac-Stark shift as a function of photon number for different orders in perturbation theory.

The spectroscopic response peaks at $\Delta = \chi_{01}\bar{n}_r$, which is proportional to the time-averaged photon number instead of the instantaneous photon number. Hence, when we fit the Kerr value K_r in Fig. 8(c), the numerical simulation results are uniformly averaged over a time window with duration T. Going to higher orders in perturbation, however, the excitation probability $P_{|1\rangle}$ depends on the specific shape of $\Omega(t)$. This leads to errors in the fitted Kerr value.

We also note that the resonator state generated by a classical drive is usually not a Fock state. The photon number discussed here should thus be thought of as a weighted average over different Fock states. In the number-splitting regime where the coupling between the transmon and the resonator is strong, $\chi_{01} > 1/T$, there is more than one peak in the spectroscopic response [45].

Appendix E: Identification of final states in the steady-state experiment

In Sec. V, we mentioned that $|6\rangle$ is one of the final states in the steady-state experiment. Here we give more details about this identification.

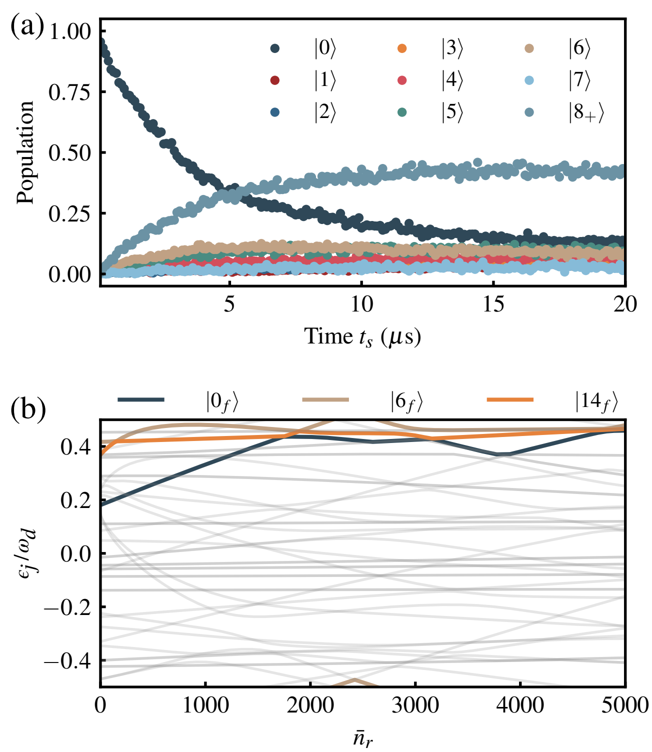

FIG. 10. Identification of final states in the steady-state experiment. (a) A linecut of the steady-state experiment results shown in Fig. 4(b) at 1500 photons. (b) Normalized Floquet quasieneregies ϵ_j/ω_d for Q_B. We take $n_g = 0$.

As shown in Fig. 10(a), we found apparent population increase in $|6\rangle$, leaving $|7\rangle$ nearly unaffected. The large population observed in states $|8\rangle$ or higher suggests that the population in state $|6\rangle$ is then further transferred to higher excited states. These observations are consistent with the Floquet analysis shown in Fig. 10(b). Following the branch $|0_f\rangle$, we encounter two nearby avoided crossings around $\bar{n}_r \sim 1800$, involving both branches $|6_f\rangle$ and $|14_f\rangle$. During the long steady-state segment, the population can be transferred to either of these branches. The $|6_f\rangle$ and $|14_f\rangle$ branches also show an avoided crossing at much lower photon number ($\bar{n}_r \sim 100$). As a result, in the experiment, the diabatic ramp-down segment leads to the population in branch $|14_f\rangle$ being assigned as $|6\rangle$ and to the population in branch $|6_f\rangle$ being assigned as $|8_+\rangle$.

Notice that the critical photon number shown in Fig. 10 is slightly larger than the measured results ($\sim$ 1500 photons) in Fig. 4. This is likely due to the effect of higher-order nonlinear terms that are accounted for in the Floquet branch analysis but not in our experimental calibration; see Appendix D 6 a.

[1] A. Blais, A. L. Grimsmo, S. M. Girvin, and A. Wallraff, Circuit quantum electrodynamics, Reviews of Modern Physics **93**, 025005 (2021).

[2] A. Blais, R.-S. Huang, A. Wallraff, S. M. Girvin, and R. J. Schoelkopf, Cavity quantum electrodynamics for superconducting electrical circuits: An architecture for quantum computation, Physical Review A **69**, 062320 (2004).

[3] J. Koch, T. M. Yu, J. Gambetta, A. A. Houck, D. I. Schuster, J. Majer, A. Blais, M. H. Devoret, S. M. Girvin, and R. J. Schoelkopf, Charge-insensitive qubit design derived from the Cooper pair box, Physical Review A **76**, 042319 (2007).

[4] V. E. Manucharyan, J. Koch, L. I. Glazman, and M. H. Devoret, Fluxonium: Single Cooper-Pair Circuit Free of Charge Offsets, Science **326**, 113 (2009).

[5] P. Krantz, M. Kjaergaard, F. Yan, T. P. Orlando, S. Gustavsson, and W. D. Oliver, A quantum engineer's guide to superconducting qubits, Applied Physics Reviews **6**, 021318 (2019).

[6] T. Walter, P. Kurpiers, S. Gasparinetti, P. Magnard, A. Potočnik, Y. Salathé, M. Pechal, M. Mondal, M. Oppliger, C. Eichler, and A. Wallraff, Rapid High-Fidelity Single-Shot Dispersive Readout of Superconducting Qubits, Physical Review Applied **7**, 054020 (2017).

[7] Y. Sunada, S. Kono, J. Ilves, S. Tamate, T. Sugiyama, Y. Tabuchi, and Y. Nakamura, Fast Readout and Reset of a Superconducting Qubit Coupled to a Resonator with an Intrinsic Purcell Filter, Physical Review Applied **17**, 044016 (2022).

[8] F. Swiadek, R. Shillito, P. Magnard, A. Remm, C. Hellings, N. Lacroix, Q. Ficheux, D. C. Zanuz, G. J. Norris, A. Blais, S. Krinner, and A. Wallraff, Enhancing Dispersive Readout of Superconducting Qubits through Dynamic Control of the Dispersive Shift: Experiment and Theory, PRX Quantum **5**, 040326 (2024).

[9] Y. Sunada, K. Yuki, Z. Wang, T. Miyamura, J. Ilves, K. Matsuura, P. A. Spring, S. Tamate, S. Kono, and Y. Nakamura, Photon-Noise-Tolerant Dispersive Readout of a Superconducting Qubit Using a Nonlinear Purcell Filter, PRX Quantum **5**, 010307 (2024).

[10] S. Hazra, W. Dai, T. Connolly, P. D. Kurilovich, Z. Wang, L. Frunzio, and M. H. Devoret, Benchmarking the readout of a superconducting qubit for repeated measurements (2025), arXiv:2407.10934 [quant-ph].

[11] R. Acharya, I. Aleiner, R. Allen, T. I. Andersen, M. Ansmann, F. Arute, K. Arya, A. Asfaw, J. Atalaya, R. Babbush, D. Bacon, J. C. Bardin, J. Basso, A. Bengtsson, S. Boixo, G. Bortoli, A. Bourassa, J. Bovaird, L. Brill, M. Broughton, B. B. Buckley, D. A. Buell, T. Burger, B. Burkett, N. Bushnell, Y. Chen, Z. Chen, B. Chiaro, J. Cogan, R. Collins, P. Conner, W. Courtney, A. L. Crook, B. Curtin, D. M. Debroy, A. Del Toro Barba, S. Demura, A. Dunsworth, D. Eppens, C. Erickson, L. Faoro, E. Farhi, R. Fatemi, L. Flores Burgos, E. Forati, A. G. Fowler, B. Foxen, W. Giang, C. Gidney, D. Gilboa, M. Giustina, A. Grajales Dau, J. A. Gross, S. Habegger, M. C. Hamilton, M. P. Harrigan, S. D. Harrington, O. Higgott, J. Hilton, M. Hoffmann, S. Hong, T. Huang, A. Huff, W. J. Huggins, L. B. Ioffe, S. V. Isakov, J. Iveland, E. Jeffrey, Z. Jiang, C. Jones, P. Juhas, D. Kafri, K. Kechedzhi, J. Kelly, T. Khattar, M. Khezri, M. Kieferová, S. Kim, A. Kitaev, P. V. Klimov, A. R. Klots, A. N. Korotkov, F. Kostritsa, J. M. Kreikebaum, D. Landhuis, P. Laptev, K.-M. Lau, L. Laws, J. Lee, K. Lee, B. J. Lester, A. Lill, W. Liu, A. Locharla, E. Lucero, F. D. Malone, J. Marshall, O. Martin, J. R. McClean, T. McCourt, M. McEwen, A. Megrant, B. Meurer Costa, X. Mi, K. C. Miao, M. Mohseni, S. Montazeri, A. Morvan, E. Mount, W. Mruczkiewicz, O. Naaman, M. Neeley, C. Neill, A. Nersisyan, H. Neven, M. Newman, J. H. Ng, A. Nguyen, M. Nguyen, M. Y. Niu, T. E. O'Brien, A. Opremcak, J. Platt, A. Petukhov, R. Potter, L. P. Pryadko, C. Quintana, P. Roushan, N. C. Rubin, N. Saei, D. Sank, K. Sankaragomathi, K. J. Satzinger, H. F. Schurkus, C. Schuster, M. J. Shearn, A. Shorter, V. Shvarts, J. Skruzny, V. Smelyanskiy, W. C. Smith, G. Sterling, D. Strain, M. Szalay, A. Torres, G. Vidal, B. Villalonga, C. Vollgraff Heidweiller, T. White, C. Xing, Z. J. Yao, P. Yeh, J. Yoo, G. Young, A. Zalcman, Y. Zhang, N. Zhu, and Google Quantum AI, Suppressing quantum errors by scaling a surface code logical qubit, Nature **614**, 676 (2023).

[12] R. Acharya, L. Aghababaie-Beni, I. Aleiner, T. I. Andersen, M. Ansmann, F. Arute, K. Arya, A. Asfaw, N. Astrakhantsev, J. Atalaya, R. Babbush, D. Bacon, B. Ballard, J. C. Bardin, J. Bausch, A. Bengtsson, A. Bilmes, S. Blackwell, S. Boixo, G. Bortoli, A. Bourassa, J. Bovaird, L. Brill, M. Broughton, D. A. Browne, B. Buchea, B. B. Buckley, D. A. Buell, T. Burger, B. Burkett, N. Bushnell, A. Cabrera, J. Campero, H.-S. Chang, Y. Chen, Z. Chen, B. Chiaro, D. Chik, C. Chou, J. Claes, A. Y. Cleland, J. Cogan, R. Collins, P. Conner, W. Courtney, A. L. Crook, B. Curtin, S. Das, A. Davies, L. De Lorenzo, D. M. Debroy, S. Demura, M. Devoret, A. Di Paolo, P. Donohoe, I. Drozdov, A. Dunsworth, C. Earle, T. Edlich, A. Eickbusch, A. M. Elbag, M. Elzouka, C. Erickson, L. Faoro, E. Farhi, V. S. Ferreira, L. F. Burgos, E. Forati, A. G. Fowler, B. Foxen, S. Ganjam, G. Garcia, R. Gasca, É. Genois, W. Giang, C. Gidney, D. Gilboa, R. Gosula, A. G. Dau, D. Graumann, A. Greene, J. A. Gross, S. Habegger, J. Hall, M. C. Hamilton, M. Hansen, M. P. Harrigan, S. D. Harrington, F. J. H. Heras, S. Heslin, P. Heu, O. Higgott, G. Hill, J. Hilton, G. Holland, S. Hong, H.-Y. Huang, A. Huff, W. J. Huggins, L. B. Ioffe, S. V. Isakov, J. Iveland, E. Jeffrey, Z. Jiang, C. Jones, S. Jordan, C. Joshi, P. Juhas, D. Kafri, H. Kang, A. H. Karamlou, K. Kechedzhi, J. Kelly, T. Khaire, T. Khattar, M. Khezri, S. Kim, P. V. Klimov, A. R. Klots, B. Kobrin, P. Kohli, A. N. Korotkov, F. Kostritsa, R. Kothari, B. Kozlovskii, J. M. Kreikebaum, V. D. Kurilovich, N. Lacroix, D. Landhuis, T. Lange-Dei, B. W. Langley, P. Laptev, K.-M. Lau, L. L. Guevel, J. Ledford, K. Lee, Y. D. Lensky, S. Leon, B. J. Lester, W. Y. Li, Y. Li, A. T. Lill, W. Liu, W. P. Livingston, A. Locharla, E. Lucero, D. Lundahl, A. Lunt, S. Madhuk, F. D. Malone, A. Maloney, S. Mandrá, L. S. Martin, S. Martin, O. Martin, C. Maxfield, J. R. McClean, M. McEwen, S. Meeks, A. Megrant, X. Mi, K. C. Miao, A. Mieszala, R. Molavi, S. Molina, S. Montazeri, A. Morvan, R. Movassagh, W. Mruczkiewicz, O. Naa-

man, M. Neeley, C. Neill, A. Nersisyan, H. Neven, M. Newman, J. H. Ng, A. Nguyen, M. Nguyen, C.-H. Ni, T. E. O'Brien, W. D. Oliver, A. Opremcak, K. Ottosson, A. Petukhov, A. Pizzuto, J. Platt, R. Potter, O. Pritchard, L. P. Pryadko, C. Quintana, G. Ramachandran, M. J. Reagor, D. M. Rhodes, G. Roberts, E. Rosenberg, E. Rosenfeld, P. Roushan, N. C. Rubin, N. Saei, D. Sank, K. Sankaragomathi, K. J. Satzinger, H. F. Schurkus, C. Schuster, A. W. Senior, M. J. Shearn, A. Shorter, N. Shutty, V. Shvarts, S. Singh, V. Sivak, J. Skruzny, S. Small, V. Smelyanskiy, W. C. Smith, R. D. Somma, S. Springer, G. Sterling, D. Strain, J. Suchard, A. Szasz, A. Sztein, D. Thor, A. Torres, M. M. Torunbalci, A. Vaishnav, J. Vargas, S. Vdovichev, G. Vidal, B. Villalonga, C. V. Heidweiller, S. Waltman, S. X. Wang, B. Ware, K. Weber, T. White, K. Wong, B. W. K. Woo, C. Xing, Z. J. Yao, P. Yeh, B. Ying, J. Yoo, N. Yosri, G. Young, A. Zalcman, Y. Zhang, N. Zhu, and N. Zobrist, Quantum error correction below the surface code threshold (2024), arXiv:2408.13687 [quant-ph].

[13] E. Jeffrey, D. Sank, J. Y. Mutus, T. C. White, J. Kelly, R. Barends, Y. Chen, Z. Chen, B. Chiaro, A. Dunsworth, A. Megrant, P. J. J. O'Malley, C. Neill, P. Roushan, A. Vainsencher, J. Wenner, A. N. Cleland, and J. M. Martinis, Fast Accurate State Measurement with Superconducting Qubits, Physical Review Letters **112**, 190504 (2014).

[14] D. Sank, Z. Chen, M. Khezri, J. Kelly, R. Barends, B. Campbell, Y. Chen, B. Chiaro, A. Dunsworth, A. Fowler, E. Jeffrey, E. Lucero, A. Megrant, J. Mutus, M. Neeley, C. Neill, P. J. J. O'Malley, C. Quintana, P. Roushan, A. Vainsencher, T. White, J. Wenner, A. N. Korotkov, and J. M. Martinis, Measurement-Induced State Transitions in a Superconducting Qubit: Beyond the Rotating Wave Approximation, Physical Review Letters **117**, 190503 (2016).

[15] Z. K. Minev, S. O. Mundhada, S. Shankar, P. Reinhold, R. Gutiérrez-Jáuregui, R. J. Schoelkopf, M. Mirrahimi, H. J. Carmichael, and M. H. Devoret, To catch and reverse a quantum jump mid-flight, Nature **570**, 200 (2019).

[16] L. Verney, R. Lescanne, M. H. Devoret, Z. Leghtas, and M. Mirrahimi, Structural Instability of Driven Josephson Circuits Prevented by an Inductive Shunt, Physical Review Applied **11**, 024003 (2019).

[17] M. Khezri, A. Opremcak, Z. Chen, K. C. Miao, M. McEwen, A. Bengtsson, T. White, O. Naaman, D. Sank, A. N. Korotkov, Y. Chen, and V. Smelyanskiy, Measurement-induced state transitions in a superconducting qubit: Within the rotating-wave approximation, Physical Review Applied **20**, 054008 (2023).

[18] R. Shillito, A. Petrescu, J. Cohen, J. Beall, M. Hauru, M. Ganahl, A. G. Lewis, G. Vidal, and A. Blais, Dynamics of Transmon Ionization, Physical Review Applied **18**, 034031 (2022).

[19] M. Lachapelle, *Mesure optimale des qubits supraconducteurs*, Master's thesis, Université de Sherbrooke (2018).

[20] J. Cohen, A. Petrescu, R. Shillito, and A. Blais, Reminiscence of Classical Chaos in Driven Transmons, PRX Quantum **4**, 020312 (2023).

[21] X. Xiao, J. Venkatraman, R. G. Cortiñas, S. Chowdhury, and M. H. Devoret, A diagrammatic method to compute the effective hamiltonian of driven nonlinear oscillators (2023), arXiv:2304.13656 [quant-ph].

[22] M. F. Dumas, B. Groleau-Paré, A. McDonald, M. H. Muñoz-Arias, C. Lledó, B. D'Anjou, and A. Blais, Measurement-Induced Transmon Ionization, Physical Review X **14**, 041023 (2024).

[23] K. N. Nesterov and I. V. Pechenezhskiy, Measurement-induced state transitions in dispersive qubit-readout schemes, Physical Review Applied **22**, 064038 (2024).

[24] S. Singh, G. Refael, A. Clerk, and E. Rosenfeld, Impact of Josephson junction array modes on fluxonium readout (2024), arXiv:2412.14788 [cond-mat].

[25] A. Bista, M. Thibodeau, K. Nie, K. Chow, B. K. Clark, and A. Kou, Readout-induced leakage of the fluxonium qubit (2025), arXiv:2501.17807 [quant-ph].

[26] A. Bengtsson, A. Opremcak, M. Khezri, D. Sank, A. Bourassa, K. J. Satzinger, S. Hong, C. Erickson, B. J. Lester, K. C. Miao, A. N. Korotkov, J. Kelly, Z. Chen, and P. V. Klimov, Model-Based Optimization of Superconducting Qubit Readout, Physical Review Letters **132**, 100603 (2024).

[27] P. D. Kurilovich, T. Connolly, C. G. L. Bøttcher, D. K. Weiss, S. Hazra, V. R. Joshi, A. Z. Ding, H. Nho, S. Diamond, V. D. Kurilovich, W. Dai, V. Fatemi, L. Frunzio, L. I. Glazman, and M. H. Devoret, High-frequency readout free from transmon multi-excitation resonances (2025), arXiv:2501.09161 [quant-ph].

[28] A. A. Chapple, O. Benhayoune-Khadraoui, S. Richer, and A. Blais, Balanced cross-kerr coupling for superconducting qubit readout (2025), arXiv:2501.09010 [quant-ph].

[29] A. A. Chapple, A. McDonald, M. H. Muñoz-Arias, and A. Blais, Robustness of longitudinal transmon readout to ionization (2024), arXiv:2412.07734 [quant-ph].

[30] G. Mainfray and G. Manus, Multiphoton ionization of atoms, Reports on Progress in Physics **54**, 1333 (1991).

[31] P. Agostini, G. Barjot, J. Bonnal, G. Mainfray, C. Manus, and J. Morellec, Multiphoton ionization of hydrogen and rare gases, IEEE Journal of Quantum Electronics **4**, 667 (1968).

[32] G. Mainfray and C. Manus, Resonance effects in multiphoton ionization of atoms, Applied Optics **19**, 3934 (1980).

[33] E. A. Martin and L. Mandel, Electron energy spectrum in laser-induced multiphoton ionization of atoms, Applied Optics **15**, 2378 (1976).

[34] Z. Deng and J. H. Eberly, Effect of Coherent Continuum-Continuum Relaxation and Saturation in Multiphoton Ionization, Physical Review Letters **53**, 1810 (1984).

[35] Z. Deng and J. H. Eberly, Multiphoton absorption above ionization threshold by atoms in strong laser fields, Journal of the Optical Society of America B **2**, 486 (1985).

[36] Z. Wang, R. W. Parker, E. Champion, and M. S. Blok, High-E_J/E_C transmon qudits with up to 12 levels, Phys. Rev. Appl. **23**, 034046 (2025).

[37] E. Champion, Z. Wang, R. Parker, and M. Blok, Multi-frequency control and measurement of a spin-7/2 system encoded in a transmon qudit (2024), arXiv:2405.15857 [quant-ph].

[38] D. Willsch, D. Rieger, P. Winkel, M. Willsch, C. Dickel, J. Krause, Y. Ando, R. Lescanne, Z. Leghtas, N. T. Bronn, P. Deb, O. Lanes, Z. K. Minev, B. Dennig, S. Geisert, S. Günzler, S. Ihssen, P. Paluch, T. Reisinger, R. Hanna, J. H. Bae, P. Schüffelgen, D. Grützmacher, L. Buimaga-Iarinca, C. Morari, W. Wernsdorfer, D. P. DiVincenzo, K. Michielsen, G. Catelani, and I. M. Pop,

Observation of Josephson harmonics in tunnel junctions, Nature Physics , 1 (2024).
[39] C. Lledó, R. Dassonneville, A. Moulinas, J. Cohen, R. Shillito, A. Bienfait, B. Huard, and A. Blais, Cloaking a qubit in a cavity, Nature Communications **14**, 6313 (2023).
[40] M. Grifoni and P. Hänggi, Driven quantum tunneling, Physics Reports **304**, 229 (1998).
[41] O. V. Ivakhnenko, S. N. Shevchenko, and F. Nori, Nonadiabatic Landau–Zener–Stückelberg–Majorana transitions, dynamics, and interference, Physics Reports **995**, 1 (2023).
[42] L. Chen, H.-X. Li, Y. Lu, C. W. Warren, C. J. Križan, S. Kosen, M. Rommel, S. Ahmed, A. Osman, J. Biznárová, A. Fadavi Roudsari, B. Lienhard, M. Caputo, K. Grigoras, L. Grönberg, J. Govenius, A. F. Kockum, P. Delsing, J. Bylander, and G. Tancredi, Transmon qubit readout fidelity at the threshold for quantum error correction without a quantum-limited amplifier, npj Quantum Information **9**, 1 (2023).
[43] N. Didier, J. Bourassa, and A. Blais, Fast Quantum Nondemolition Readout by Parametric Modulation of Longitudinal Qubit-Oscillator Interaction, Physical Review Letters **115**, 203601 (2015).
[44] A. Brinkmann, Introduction to average Hamiltonian theory. I. Basics, Concepts in Magnetic Resonance Part A **45A**, e21414 (2016).
[45] D. I. Schuster, A. A. Houck, J. A. Schreier, A. Wallraff, J. M. Gambetta, A. Blais, L. Frunzio, J. Majer, B. Johnson, M. H. Devoret, S. M. Girvin, and R. J. Schoelkopf, Resolving photon number states in a superconducting circuit, Nature **445**, 515 (2007).